Cornell University

Ionospheric Measurement Techniques

Michael C. Kelley

School of Electrical and Computer Engineering

Techniques Classification

1. Radio Wave Techniques
   - 1.1. Incoherent Scatter Radars (ISR)
   - 1.2. Coherent Scatter Radars (CSR)
   - 1.3. Scintillation Techniques
2. Optical Methods
   - 2.1. Airglow
   - 2.2. Lidar
   - 2.3 Fabry-Perot Interferometry
3. In Situ Measurements
   - 3.1. Langmuir Probes, Retarding Potential Analyses, and Drift Meters
   - 3.2. Electric Current, Measurements - The Fluxgate Magnetometers
   - 3.3. Double-Probes, Electric Field Detectors
   - 3.4. Electrostatic Waves Measurements
   - 3.5. Barium Ion Cloud Measurements

ISR Radar Sites

The ground was broken for the first incoherent scatter radar (ISR) site in Arecibo, Puerto Rico, in 1959. At the time of writing, there are 15 such sites. The locations of many of these sites are given in Table A.1 along with other relevant information.

Table A.1 Relevant Parameters and Coordinates

Observatory	Frequency (MHz)	Geographic Latitude	Geographic Longitude	*L*	UT–LT
Jicamarca, Peru	49.9	11.9°S	76°W	1.05	5
Altair, Kwajalein	155.5	8.8°N	167.5°E	1.1	−11
MU, Japan	46.5	34.85°N	136.10°E	1.33	−9
Arecibo, Puerto Rico	430	18.3°N	66.75°W	1.43	4
St. Santin, France*	935	44.6°N	2.2°E	1.76	0
Millstone Hill, Massachusetts	440	42.6°N	71.5°W	3.12	5
Chatanika, Alaska*	1290	64.9°N	147.7°W	5.51	10
Poker Flat ISR (PFISR)	450	64.9°N	147.7°N	5.51	10
EISCAT (Tromso, Norway)	224/933	69.6°N	19.2°E	6.3	−2
Sondre Stromfjord, Greenland	1290	67.0°N	50.95°W	15+	3
EISCAT Svalbard Radar	500	78.1°N	15.1°E	20+	−1
Resolute Bay (Nunavit, Can.)**	450	75.0°N	95.0°E	100+	−6 hr

*Decommissioned; **Under construction.

The Backscatter Spectrum

The original idea (Gordon, 1958) hypothesized quite naturally that the Doppler width of the returned spectrum would be of order

$$\delta f / f \cong \langle V \rangle_e / c$$

where $<V>_e$ is the mean thermal electron velocity. Surprisingly, the first experiments, by Bowles (1958), showed the Doppler width to be of order $<V_i>/c$, where $<V_i>$ is the ion thermal speed. This is explained by the fact that, when the probing wavelength is greater than the Debye length, the electrons are linked to the ions through the Debye cloud around them, and part of the scattered signal (the ion line) is characterized by ion properties.

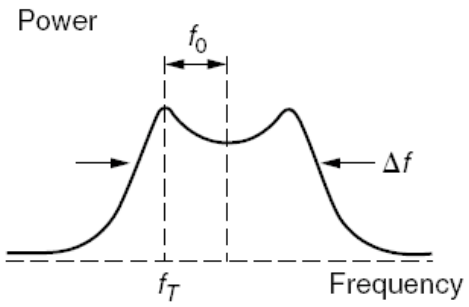

f_T gives the line-of-sight component of the mean ion velocity $\mathbf{V}_i$. If several positions are used, the complete vector flow velocity can be found. In the F region the ion flow velocity yields the perpendicular electric field components via the relationship $\mathbf{E}_\perp = \mathbf{B} \times \mathbf{V}_i$

The ion flow velocity parallel to **B** is much more complicated, since many factors contribute, such as the component of the neutral wind along **B**, the ion pressure gradient, and gravitational forces.

The Theory

The theory of scattering from thermal fluctuations is very well understood. In fact, as pointed out by Farley (1979), when viewed as a test of the crucial Landau damping method for carrying out Vlasov plasma theory, measurements of the incoherent scatter spectrum have verified that method to better than 1% accuracy. The radar scatters from irregularities in the medium, km, according to the relationship $\mathbf{k}_T = \mathbf{k}_s + \mathbf{k}_m$ where $\mathbf{k}_T$ is the transmitted wave and $\mathbf{k}_s$ the scattered wave. Since $\mathbf{k}_s = -\mathbf{k}_T$ for backscatter,

$$\mathrm{k}_m = 2\mathrm{k}_T \qquad \lambda_m = \frac{4\pi}{\lambda}$$

Thus, the scattering wavelength is one-half the transmitted wavelength. Equation represents conservation of momentum since each photon carries a momentum equal to $\hbar\mathbf{k}$. Conservation of energy (each photon energy equal to $\hbar\omega$) requires $\omega_T = \omega_s + \omega_m$ Thus, the Doppler width of the returned spectrum ($\omega_s - \omega_T$) is related to the frequencies of waves in the medium, ω_m. Since thermal fluctuations can be considered as a superposition of damped sound waves, the spread in ω_m is of the order $\omega_m \approx |\mathbf{k}_m| C_s$ where Cs is the sound speed in a plasma, $C_s^2 = (kT_e + kT_i)/M_i$

The width of the ion line for a 50MHz radar in a plasma with $C_s \approx 1000$m/s is thus of order [$(4\pi/6)$ m](1000m/s) $\approx$ 4000 rad/s $\approx$ 600 Hz. For a medium of the same temperature the Doppler width will just scale with the radar frequency, so at Arecibo (430 MHz) the width of the "ion line" is about eight times larger.

The Full Spectrum

The first simultaneous observations of both ion and electron scattering lines (called plasma lines). The data were taken in the altitude range 1460–2486km over Arecibo, where H+ is the dominant ion.

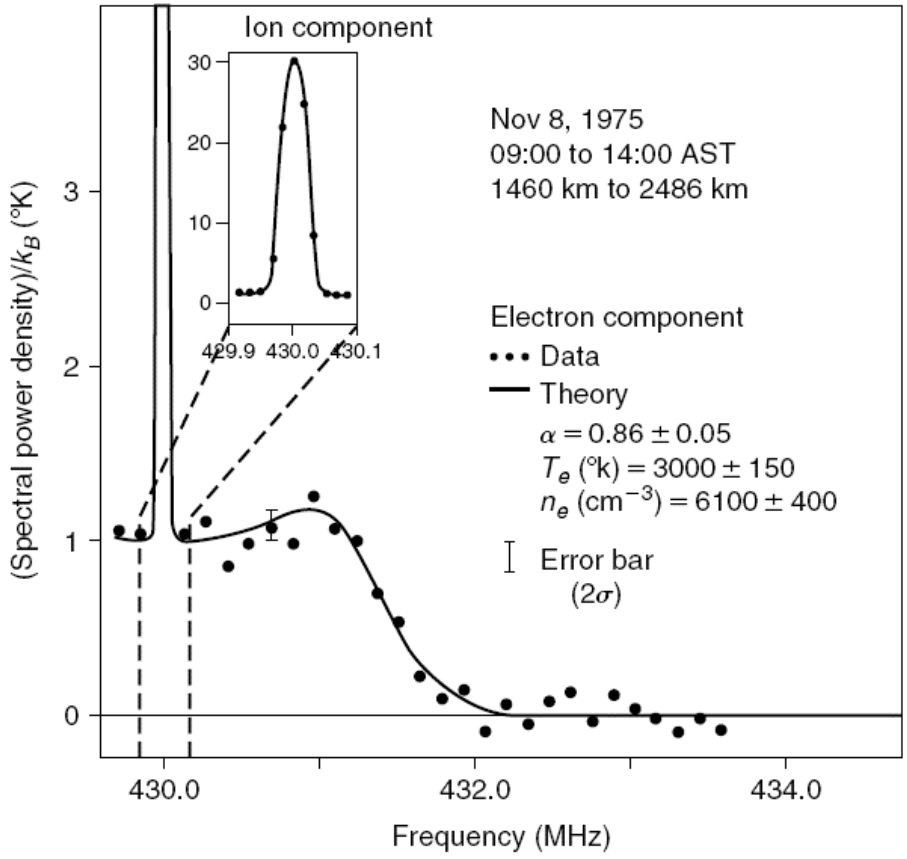

Plasma and Gyro Lines

The plasma and the gyro lines as a function of time near 200km. The latter is an electrostatic wave in a magnetized plasma that also exists in thermal equilibrium related to the whistler mode electromagnetic branch.

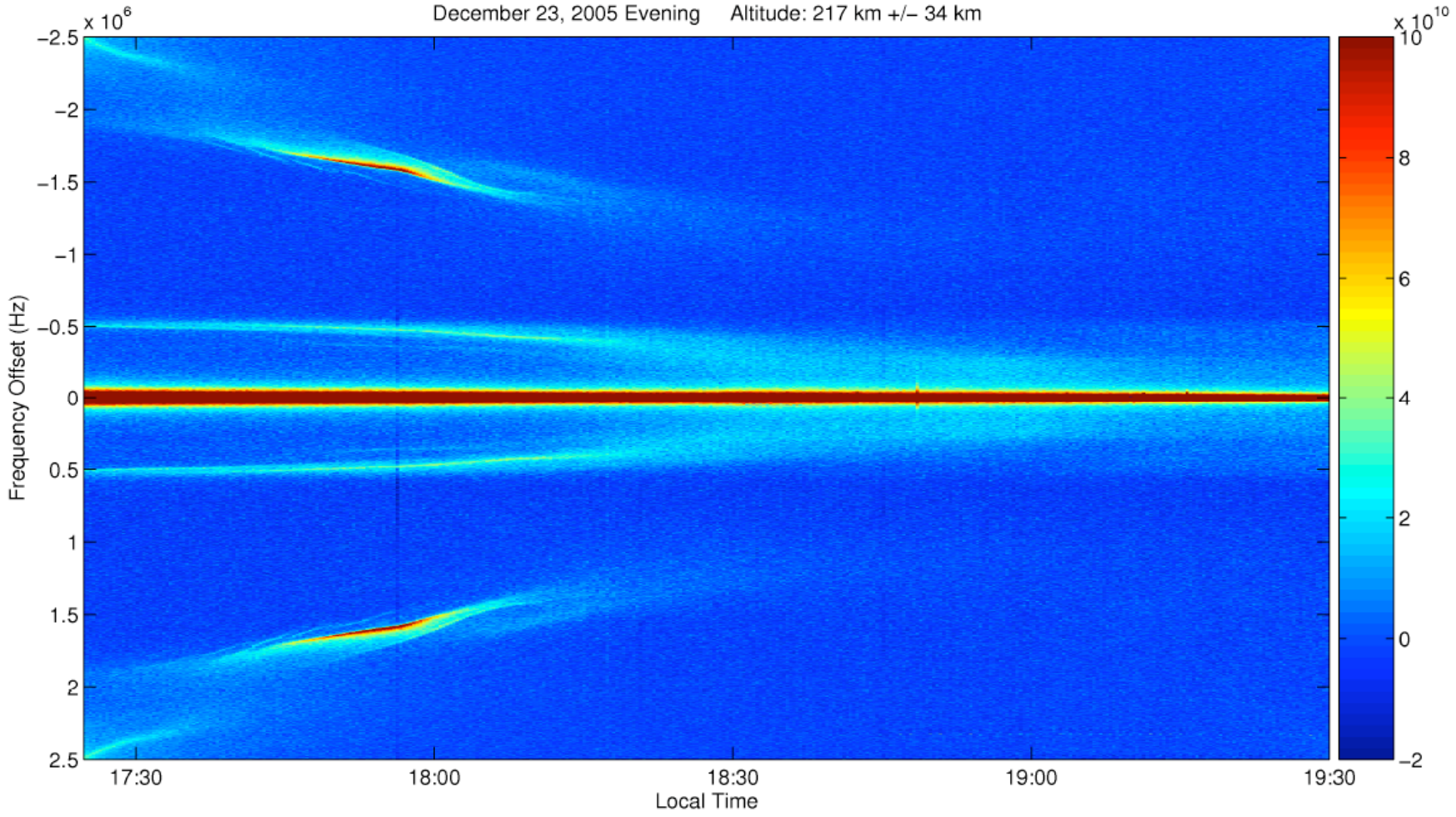

The Autocorrelation Function (ACF)

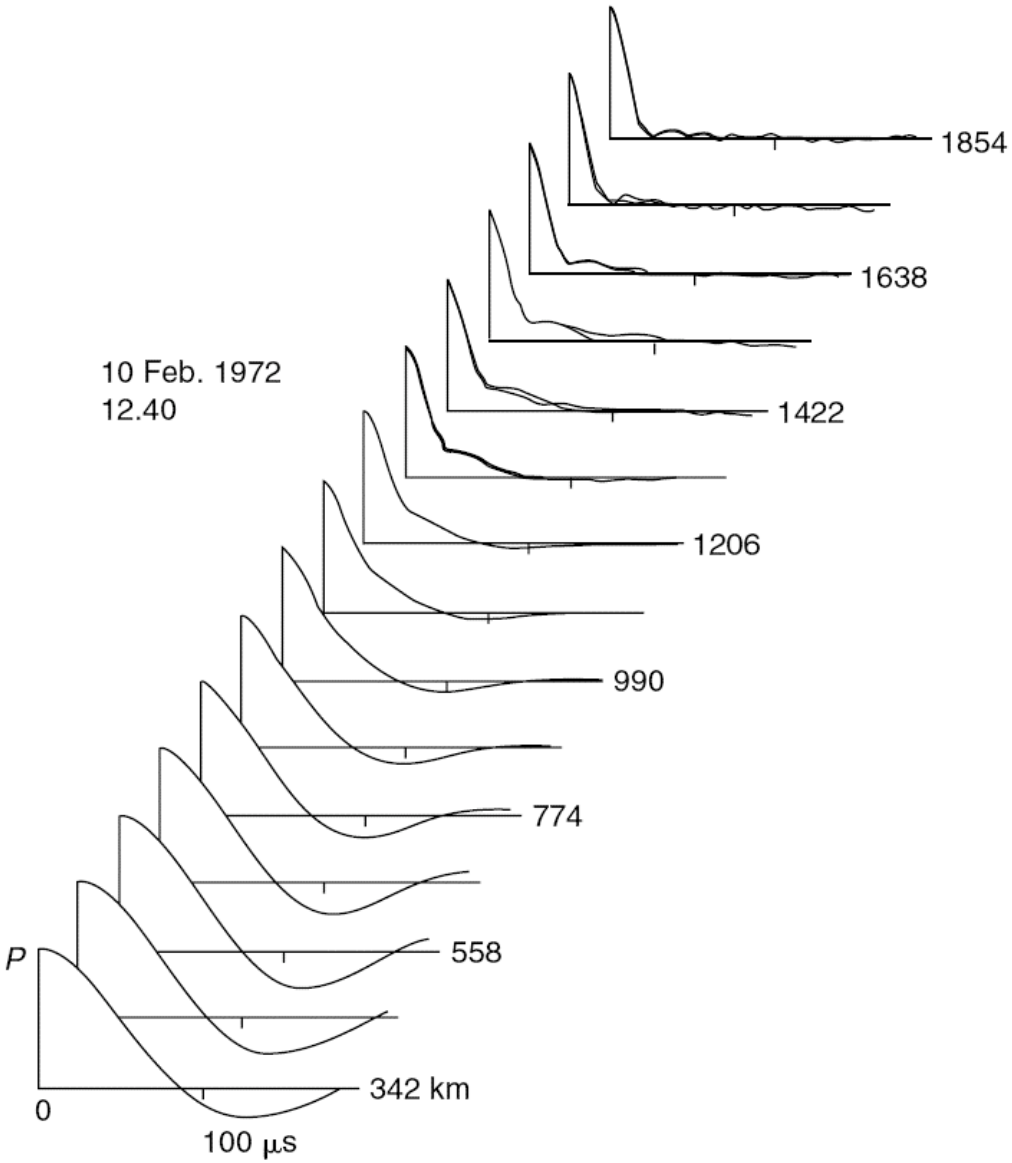

In practice, most ISR systems measure the temporal autocorrelation function of the signals scattered from a fixed point in space by sending up a series of pulses. Since the spectrum is the Fourier transform of the autocorrelation function (ACF), it can be generated at will on the ground using the latter. The temporal resolution is then determined by how many such measurements must be averaged to generate a reasonable ACF. Since the theory is exact, least-squares fitting methods can be used on the ACF waveform which include second-order ion species, differential drifts of the various ions, and so forth. This further increases the information on the ionosphere available via the ISR method.

1. Small radars get echoes when non-thermal irregularities exist at Bragg Scale
2. Equatorial & auroral electrojets
3. Sporadic E layers at mid-latitudes
4. Corretive Ionospheric S forms
5. MSTID's
6. PMSE

Coherent Scatter Radars (CSR)

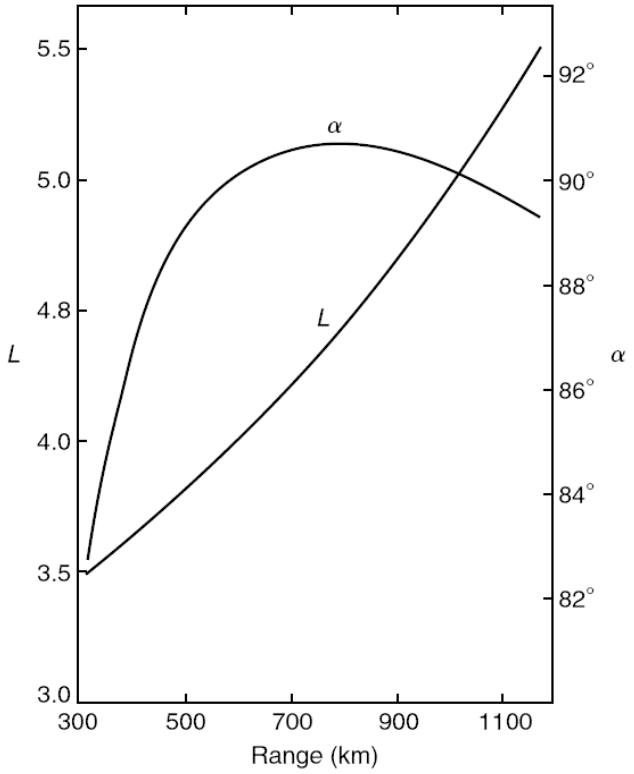

CSR Interferometry

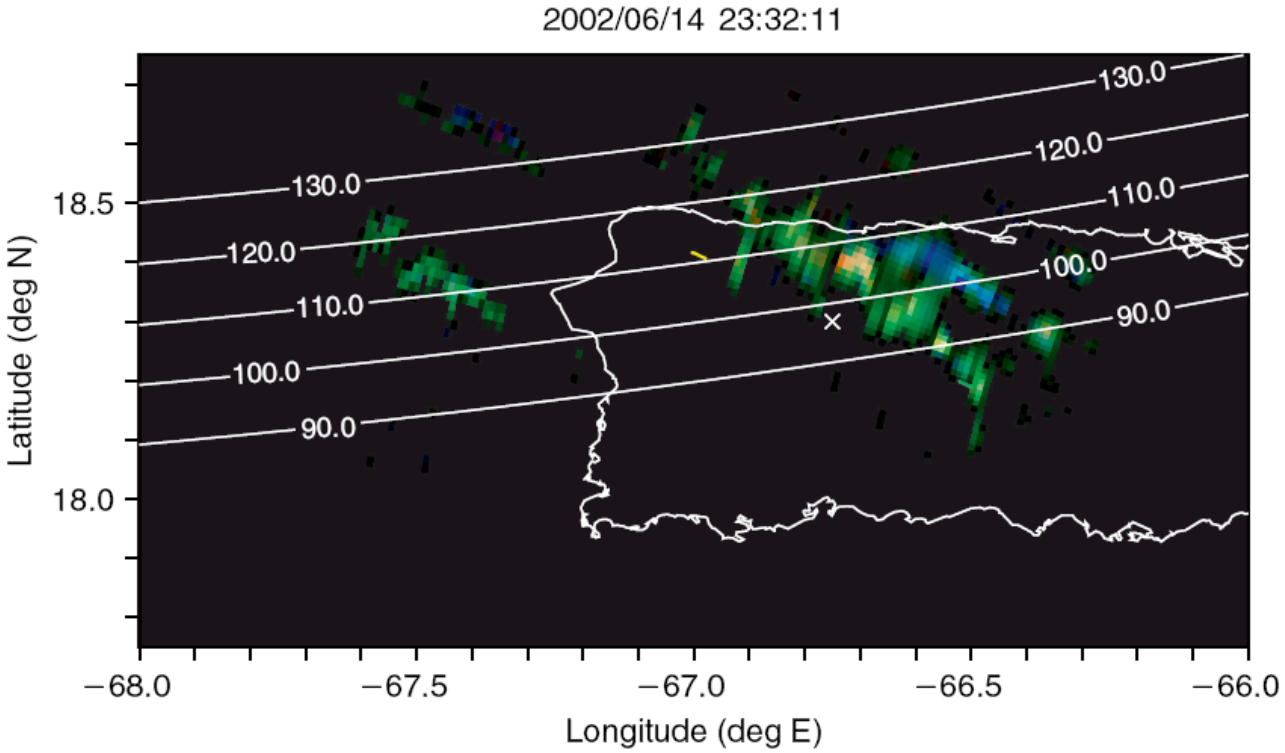

$$S_{EW}(\omega) = \frac{\langle F_E(\omega) F_w^*(\omega) \rangle}{\langle |F_E(\omega)|^2 \rangle^{1/2} \langle |F_W(\omega)|^2 \rangle^{1/2}}$$

Scintillation Techniques

The scintillation method is used to study the ionosphere by measuring the fluctuations of a radio signal due to its traversal through an irregular medium. In this method, the medium is considered to be equivalent to a diffracting screen with random density irregularities which are frozen in the uniform background and move with a fixed velocity.

In the weak-scattering, thin-screen approximation, the medium is replaced by a plane surface along which the phase of the radio wave fluctuates but the amplitude remains constant. As the wave propagates beyond the screen, fluctuations in amplitude begin to develop, due to interference effects. Let $P_\phi(k_x, k_y)$ be the power spectrum of the phase fluctuations in the wave emerging from an irregularity layer and $P_I(k_x, k_y)$ be the power spectrum of the intensity fluctuations in the received signal, expressed in a reference frame with the k_z axis aligned with the direction of the incident wave. It has been shown (Bowhill, 1961; Rufenach, 1975; Salpeter, 1967) that the following relations apply in the weak-scattering limit:

$$P_\phi(k_x, k_y) = 2\pi(r_e\lambda)^2(L\sec\psi)P_N(k_x, k_y, k_z = 0)$$

$$P_I(k_x, k_y) = 4\sin^2\left[\left(k_x^2 + k_y^2\right)/k_f^2\right]P_\phi(k_x, k_y)$$

Scintillation measurements of P_ϕ and P_I thus yield information on the twodimensional wave number spectrum of electron density fluctuations in the ionospheric plasma.

Optical Methods

A variety of passive and active optical methods exist for aeronomical studies. Aurora can be detected with the naked eye, as can noctilucent clouds, long-lived meteor trails, and intense mesospheric bores. The figure shows the wavelength coverage of various methods.

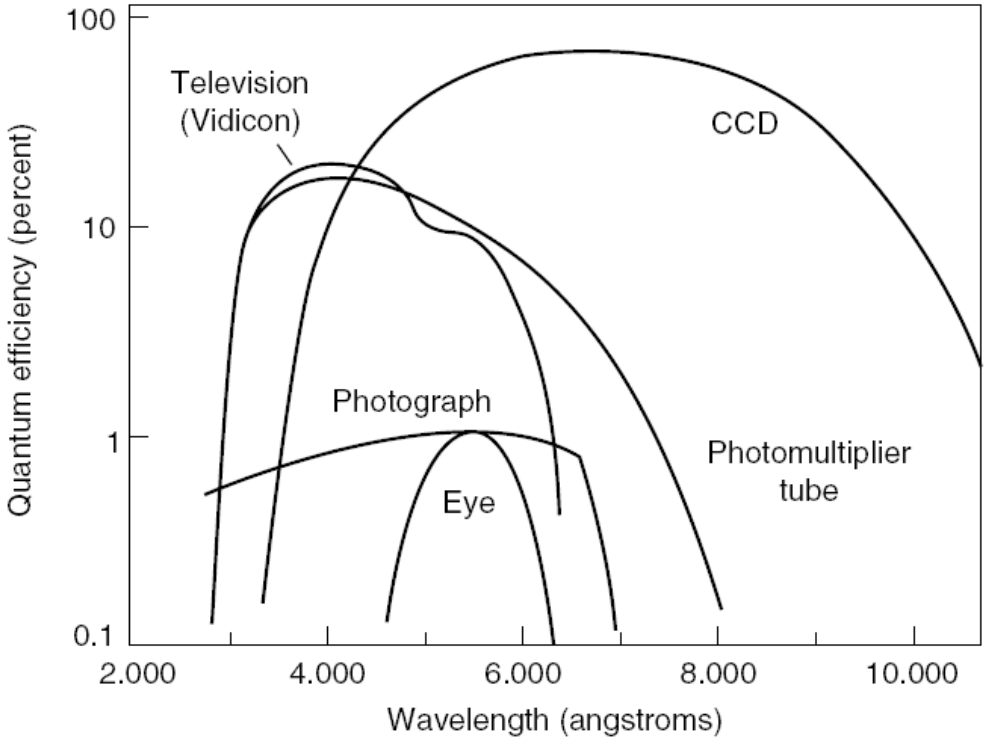

Airglow

Airglow intensity is measured in flux of photons per unit area per second. The standard unit of measure is the Rayleigh which corresponds to 106 photons/cm2 ·s and is named in honor of Robert John Strutt, the fourth Lord Rayleigh (the term "Rayleigh Scattering" is named in honor of his father, the third Lord Rayleigh). The Rayleigh unit is convenient for airglow because of its relationship with the volume emission rate V. V is defined as the emission per unit volume per unit time in photons/cm3/s, and is given by:

$$V = k_r [A^*]$$

where k_r is the rate coefficient, and $[A*]$ is the concentration of the excited chemical specie A.

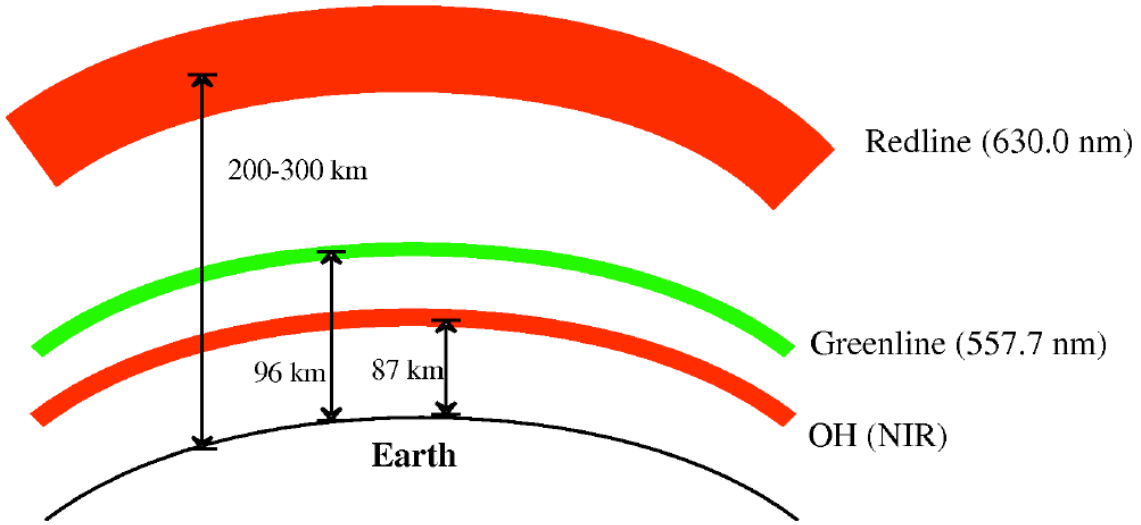

The 557.7 nm Emission

The green line emission was one of the first airglow emissions to be discovered and, as far back as 1923 (Bates, 1981) it was known that the emission is due to the transition:

$$O(^1S) \rightarrow O(^1D) + h\nu(\lambda = 557.7\,\text{nm})k_g$$

Since the preceding transition results in atomic oxygen in the O(¹D) state, one might expect a 5577 emission to be immediately followed by a 6300 emission because the 6300 emission comes from the O(¹D) state (see the next section). The reason this does not occur is due to the long lifetime of the O(¹D) state (110 s) (Rishbeth and Garriot, 1969). At the height of the 5577 emission, collisions are so frequent that the O(¹D) state is deactivated well before it can radiate a red photon.

The source of the excited O(¹S) is now generally accepted to be the two-step Barth mechanism, given by

$$O + O \xrightarrow{M} O_2^* \quad \alpha_1 \qquad O + O_2^* \rightarrow O\left(^1S\right) + O_2 \quad \beta_1$$

which requires a collision with a third-body M (most probably N_2). The rate coefficients are given by k_g, α_1, and β_1. the emission rate is proportional to the cube of the concentration of atomic oxygen. Figure A.7 plots this function using data from the MSIS-86 model. The bulk of the concentration of O lies between 95km and 100km and therefore explains the origin of the emission as a layer.

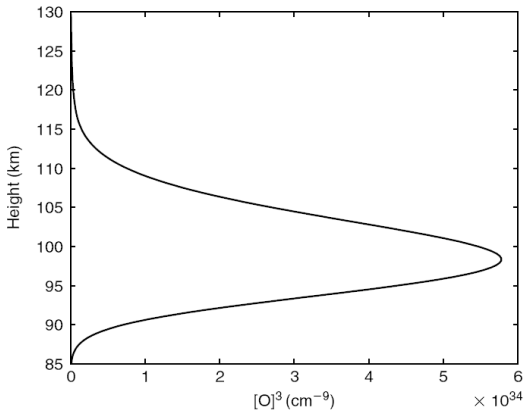

The NIR OH Broadband Emission

The vibrationally excited OH species arise from a reaction involving atomic hydrogen and ozone:

$$H + O_3 \rightarrow OH + O_2 + kJ \cdot mol^{-1}$$

The figure shows a graph of the relative intensities of the different OH lines from 725.1 nm to 896.2 nm. These are the values as computed by Meinel (1950), who first identified OH in the airglow spectrum. The OH emission bands subsequently became known as the *Meinel Bands* in honor of this scientist.

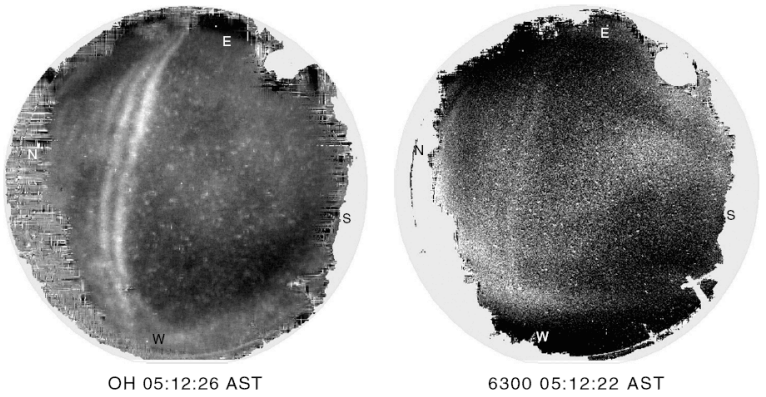

Swenson and Gardner (1998) have developed a model for calculating the volume emission rate of the OH(8,3) transition at ~737 nm.

$$V(8,3) = \frac{K_1[O][O_2]^2(200/T)^{2.5}}{1 + K_2[O_2]}$$

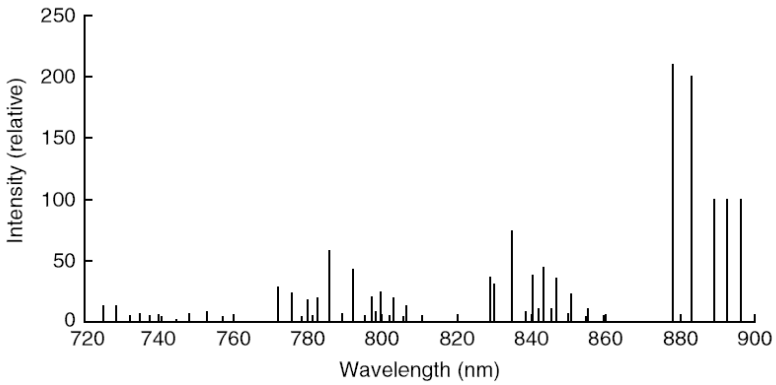

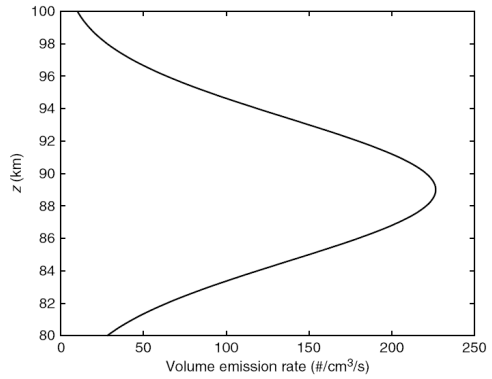

The 630 Emission

The 630.0 nm emission is an effective although complicated tracer for the dynamics of the ionosphere near the peak of the F region (250–300km). Its volume emission rate is dependent on both the electron density and the neutral O_2 density, and so its peak emission altitude follows the rise and fall of the F layer, with the peak emission altitude in general lying *below* the F peak. Furthermore, the emission intensity drops off dramatically with altitude if the F layer rises. This effect is easily confused with decreasing intensity due to a drop in electron content. The 630.0 nm emission arises from the transition:

$$O(^1D) \rightarrow O(^3P) + h\nu(\lambda = 630.0\,\text{nm})$$

The $O(^1D)$ state is populated by dissociative recombination of O^+_2, which itself arises from a collisional charge transfer between neutral molecular oxygen and ionized atomic oxygen.

$$O^+ + O_2 \rightarrow O_2^* + O \quad k_1$$

$$O_2^+ + e \rightarrow O(^1D) + O(^3P) + 4.49\,\text{eV} \quad \alpha$$

The 630 Emission

It is also possible for dissociative recombination to produce oxygen in the O(^{1}S), but experimentally it has been shown that it is a small fraction (~15%) of the O(^{1}D), so it has generally been ignored as a source for O*(1S)* (Rishbeth and Garriott, 1969). With the CU Imager, however, we have seen that the thermospheric contribution to the O(^{1}S) state can be considerable when electron densities are high. The figure shows raw images taken with the 557.7, 630.0, and background filters the night of February 17, 1998.

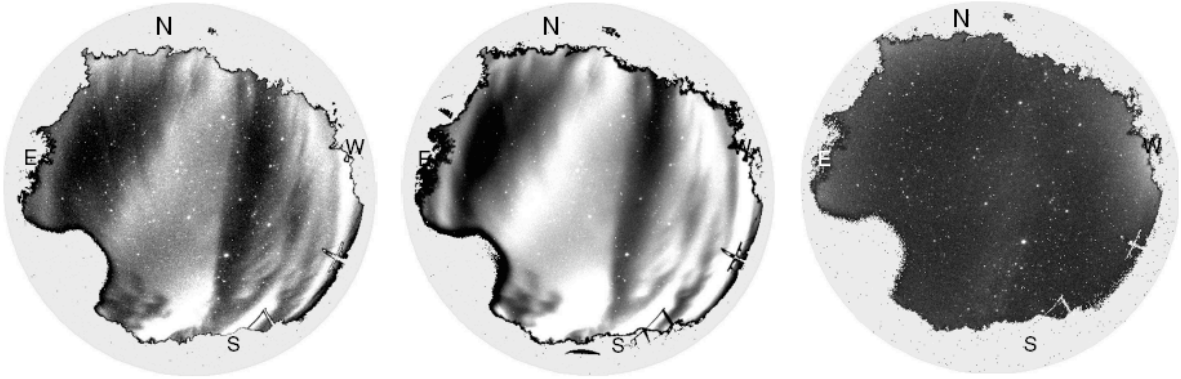

The competing reactions for the loss of the O(^{1}D) state arise from collisions with N_2, O_2, and free electrons.

$$O(^1D) + N_2 \rightarrow O(^3P) + N_2 \quad k_2$$

$$O(^1D) + O_2 \rightarrow O(^3P) + O_2 \quad k_3$$

$$O(^1D) + e \rightarrow O(^3P) + e \quad k_4$$

The 630 Emission

The figure below show more realistic profiles for the concentrations of N2 and O2 by using the MSIS-86 model. The total airglow intensity viewed from the ground is given by the height integral of the volume emission rate. It is clear that if the electron density profile were to rise the airglow intensity would fall because of the exponential drop-off of the O2 concentration. For the same reason the intensity would increase if the electron density profile fell. Therefore, intensity variations in the 630.0nm emission are in many instances associated with fluctuations in the height of the F peak. Note that the peak of the volume emission rate is approximately 50km below the peak in electron density.

It is also important to note that the half-width of this emission is almost an order of magnitude larger than those of the mesospheric emissions. The form of (A.26) is very similar to that for the Pedersen conductivity and can be used to determine that parameter (Makela and Kelley, 2003).

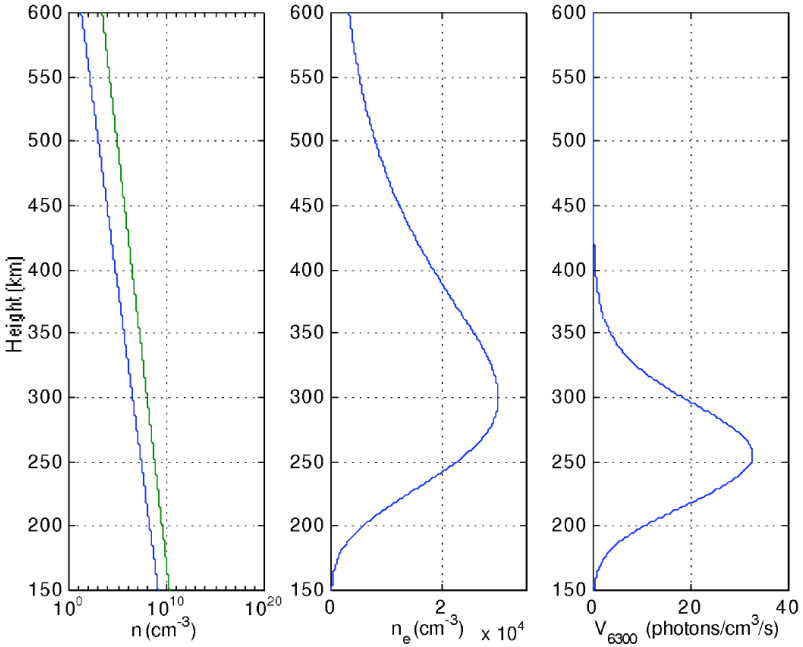

Oxygen Recombination Lines

The reaction $O^+ + e^- \rightarrow O + h\nu$ is very slow because it is difficult to conserve energy momentum in this type of reaction. Several emissions can occur in this reaction, only one of which is detectable on the ground—that is, at 774 nm. The TIMED satellite uses the 139.4nm emission. The equatorial arcs are plainly visible, as are striations due to depleted plasma wedges due to CIS/ESF. The figure also shows a simultaneous 777.4nm emission taken from Hawaii, which were used to identify the depleted light regions. For an O^+ plasma, the emission is proportional to $(n_e)^2$ and so is independent of height. A combination of 630nm and 777.4nm can thus be used to determine the height of the ionosphere (Makela et al., 2001).

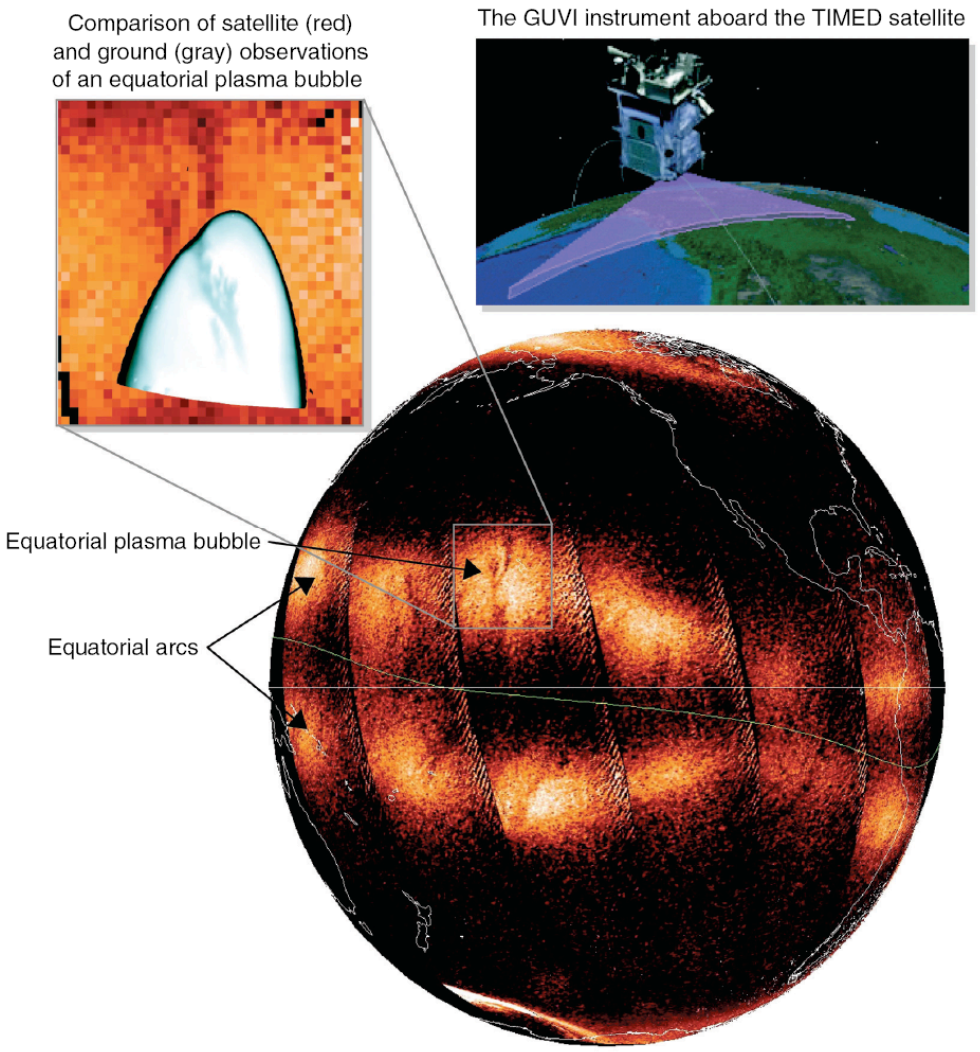

Rayleigh and Resonance Scatter

A Rayleigh lidar scatters from molecules in the atmosphere. The cross section thus decreases exponentially with altitude. Resonance lidars use resonant (fluorescence) scattering from metallic atoms that have a cross section many orders of magnitude larger than the atmosphere at typical heights where the atoms are found. Using such scatterers extends the useful height of the lidar method.

Mie scatter occurs when the particle size moves out of the Rayleigh range into a size comparable to the lidar wavelength. The most important Mie scatter is from noctilucent clouds

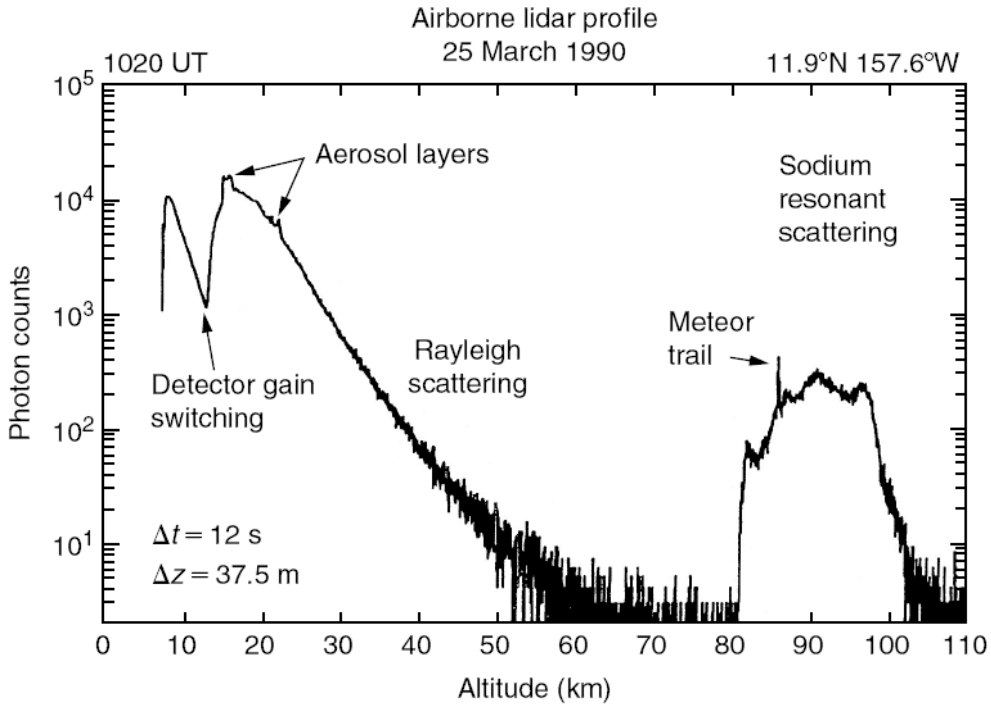

Schematic of a Fabry-Perot Interferometer (FPI)

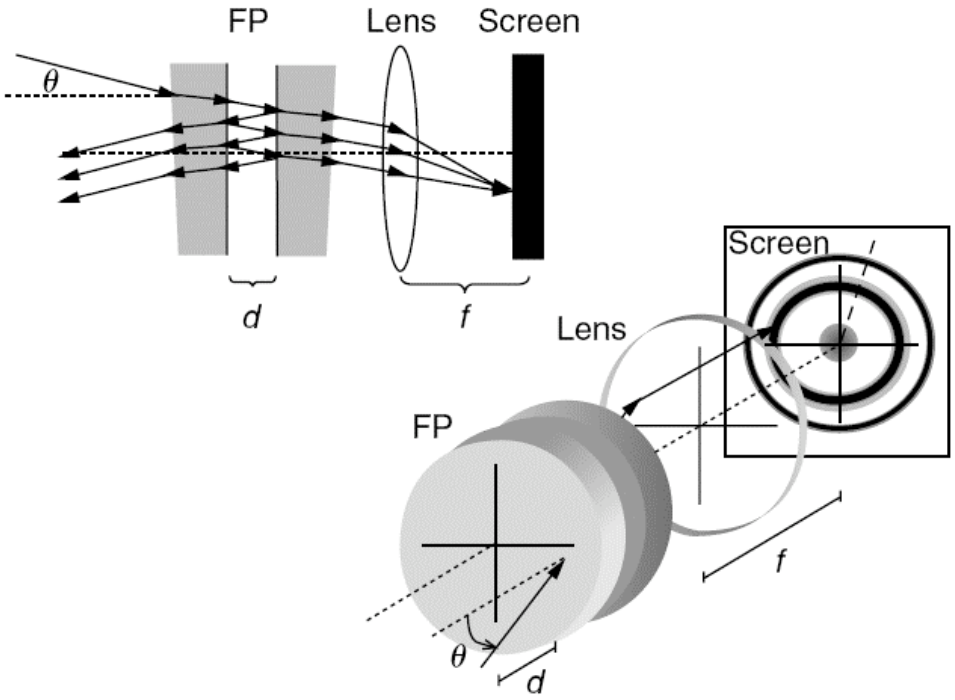

FPI Data

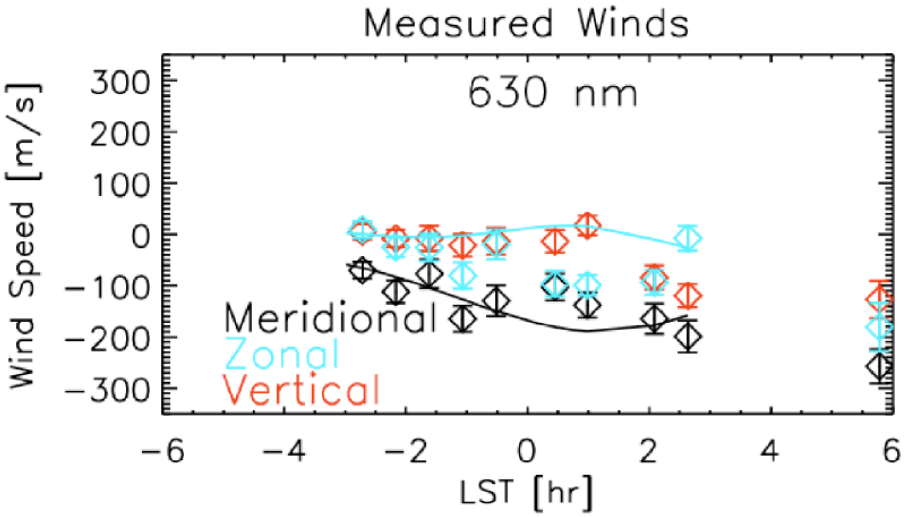
Measured Winds
630 nm
Wind Speed [m/s]
300
200
100
0
−100
−200
−300
Meridional
Zonal
Vertical
−6
−4
−2
0
2
4
6
LST [hr]

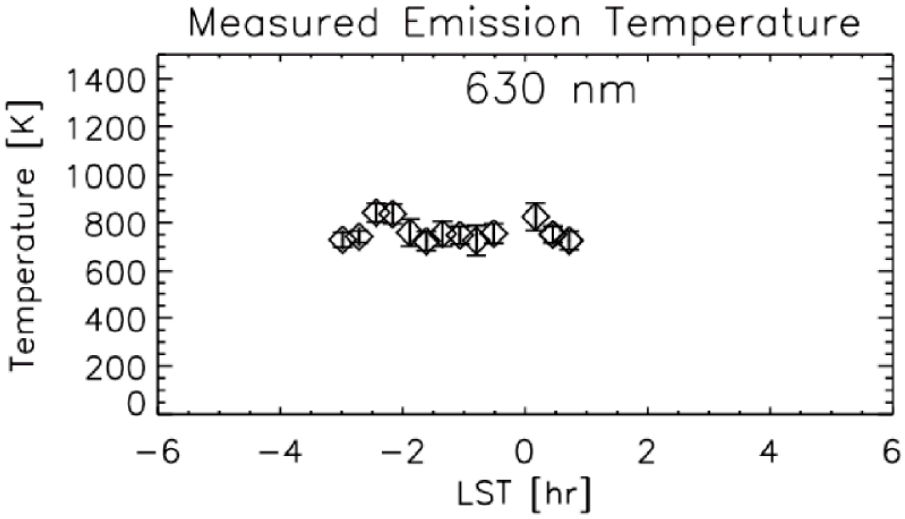
Measured Emission Temperature
630 nm
Temperature [K]
1400
1200
1000
800
600
400
200
0
−6
−4
−2
0
2
4
6
LST [hr]

The Langmuir Probe: Electron Temperature Measurements

Most Langmuir probes consist of small conducting surfaces with cylindrical or spherical geometries. The instruments function by applying a varying voltage to the probe that covers the range of energies of interest. Typical probe voltages may vary between +5 and −5 V. In the electron retardation region the probe current is given by

$$I_e = N_e q A \left(k_B T_e / 2\pi m_e\right)^{1/2} \exp(-q\Phi / k_B T_e)$$

In the two saturation regions, the ion current and the electron current can be obtained by integrating the appropriate drifting Maxwellian energy distribution function over the collector surface for all energies less than the probe potential. In the so-called electron saturation region the electron current to a cylindrical collector is given approximately by

$$I_e = 2AN_e q \left(\frac{k_B T_e}{2\pi m_e}\right)^{1/2} \frac{1}{\pi^{1/2}} \left(1 + \frac{q\Phi}{k_B T_e}\right)^{1/2}$$

Typical Langmuir probe I-V characteristic

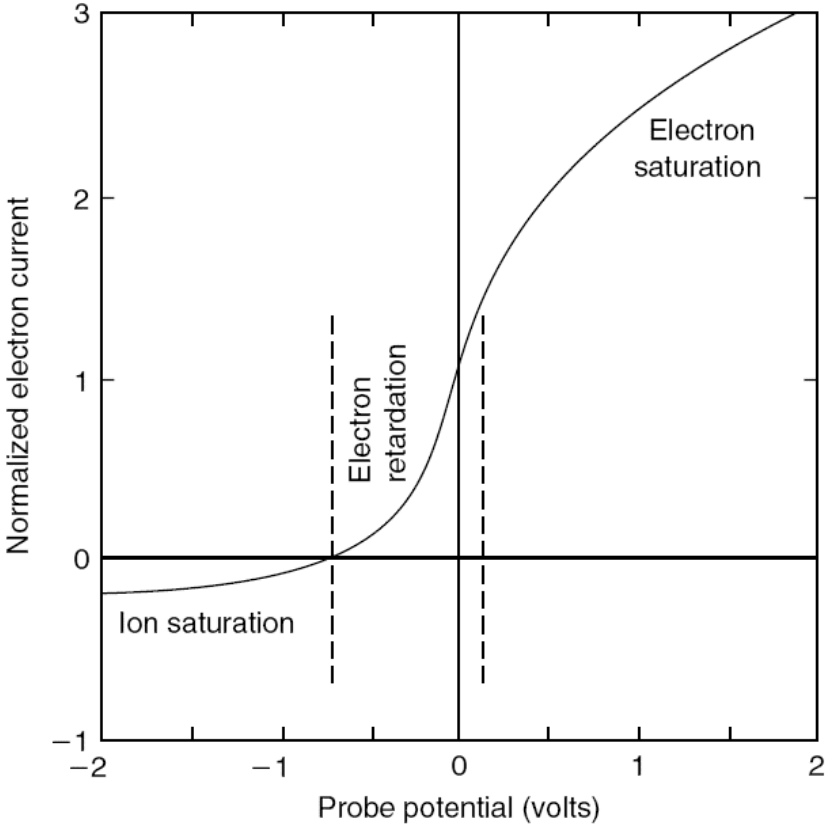

The Retarding Potential Analyzer (RPA): Ion Temperature and Density Measurements

Grid arrangement for a plasma retarding potential analyzer

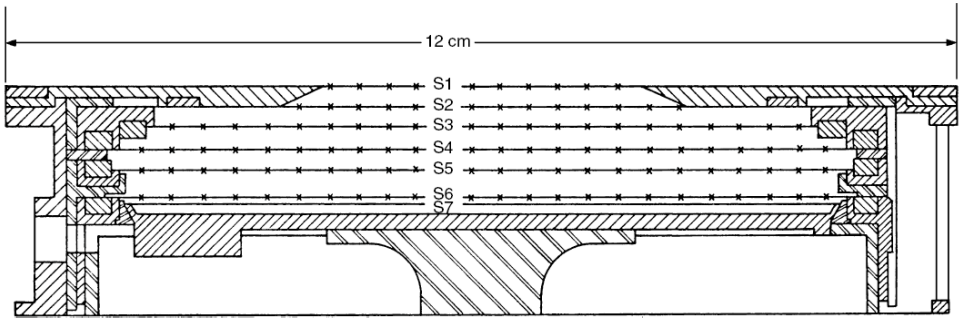

The ion current at a given retarding potential depends on the ion flux reaching the collector for all ion species with energy greater than the applied potential. This quantity can be obtained by integrating the ion velocity distribution function over the collector surface. The simplest expression is obtained for a planar surface and is given by

$$I = \frac{1}{2}\alpha V A_q \sum_i N_i \left[1 + erf(\beta_i f_i) + \frac{1}{\pi^{1/2}\beta_i V}\exp\left(\beta_i^2 f_i^2\right)\right](\hat{n}\cdot\mathbf{v})$$

where

I = collector current
α = grid transmission factor
A = aperture area
N_i = concentration of ith ion
$V = \mathbf{v}\cdot\hat{n}$
$\beta_i = (m_i/2k_BT_i)^{1/2}$
m_i = mass of ith ion
T_i = ion temperature
$\hat{n}$ = unit vector normal to sensor face
$\mathbf{v} = \mathbf{v}_d - \mathbf{v}_p$
$\mathbf{v}_p$ = sensor velocity
$\mathbf{v}_d$ = ambient ion drift velocity
$f_i = V - [2q(\Phi + \Phi_0)/m_i]^{1/2}$
k_B = Boltzmann constant
Φ = retarding grid potential
Φ_0 = spacecraft potential

Sample of RPA curves for various ionospheric conditions

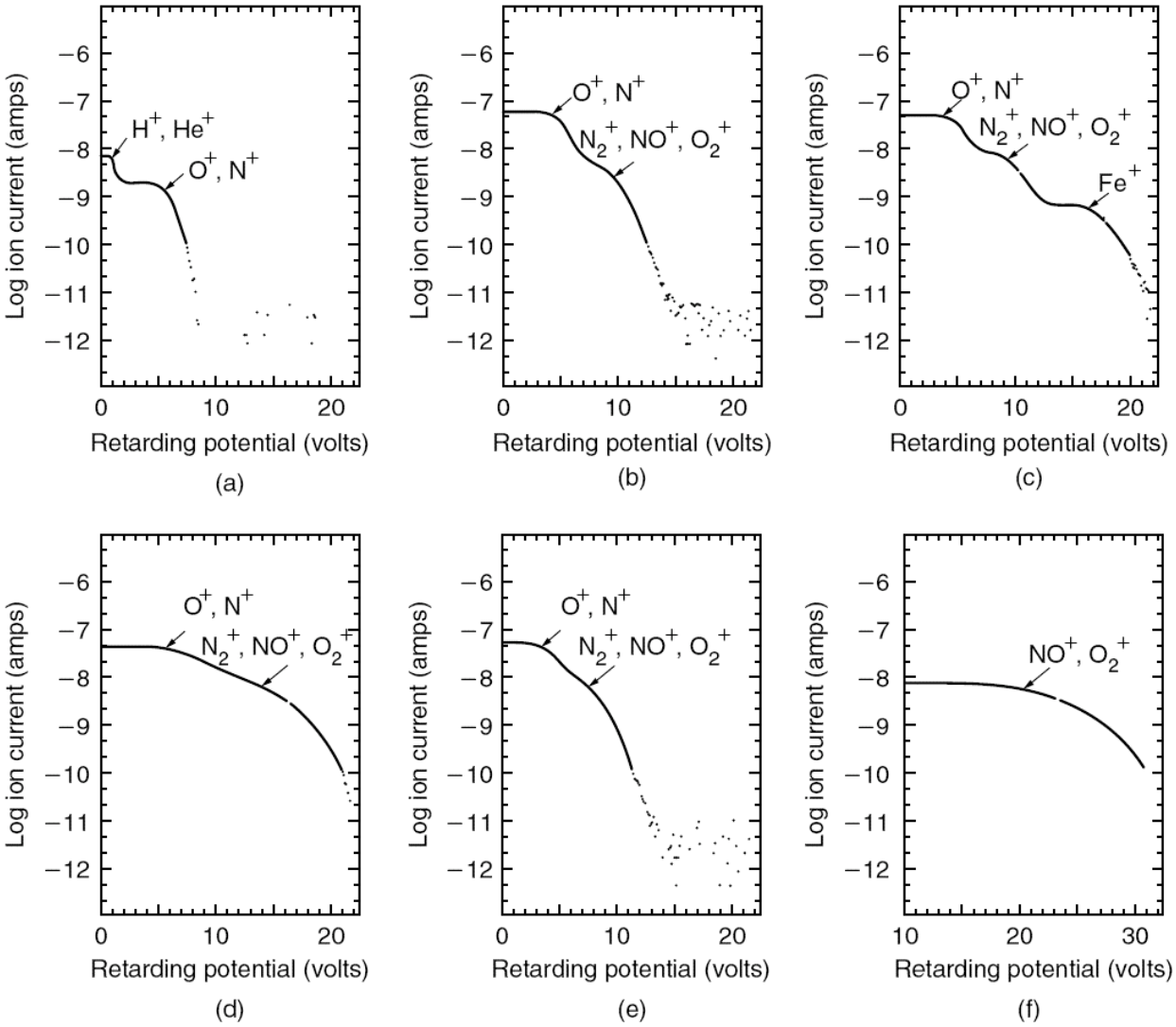

The Ion Drift Meter (IDM): Ion Drift Velocity Measurements

Modification of a plasma ion sensor to measure the plasma drift velocity

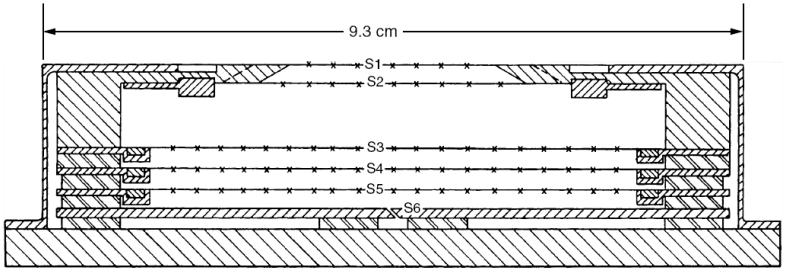

We have seen that a planar RPA is capable of measuring the component of the ion drift velocity along the look direction of the sensor. In the earth's ionosphere, where an orbiting spacecraft moves at a velocity much larger than the ion thermal speed, a rather simple device called an ion drift meter (IDM) can be used to measure the other two mutually perpendicular ion drift velocity components. The IDM has a planar geometry similar to the RPA but has a square entrance aperture and a segmented collector.

The grid S5 is biased negatively to prevent ambient electrons from reaching the collector and to suppress any photoelectrons liberated from the collector surface. All other grids are grounded to ensure a field-free region between S2 and S3 through which the ambient ions can drift. Since the ions are moving supersonically with respect to the sensor, they form a collimated beam in the manner shown in above figure. The collector area which they illuminate will therefore depend on the angle at which they arrive at the sensor. Since the current collected on each collector segment is proportional to the area struck by the ion beam, it can be shown quite easily that the ratio of the currents of two segments is proportional to the tangent of the ion arrival angle.

IDM: Geometrical interpretation of measured particle arrival angles

If the entrance aperture has straight edges and the currents to each collector pair are denoted by I_1 and I_2, then

$$\log I_1 - \log I_2 = \log(I_1/I_2) = \log\left[(H + D\tan\alpha)/(H - D\tan\alpha)\right]$$

If we let $I_1 - I_2 = I$ and let $I = I_1 + I_2$, then to first order in $\Delta I/I$ we can show that

$$\log I_1 - \log I_2 = (2H/D)\tan\alpha$$

Thus, by using a combination of logarithmic amplifiers to measure the collector current and a linear difference amplifier to supply the difference in the signals, it is possible to obtain the ion arrival angle directly.

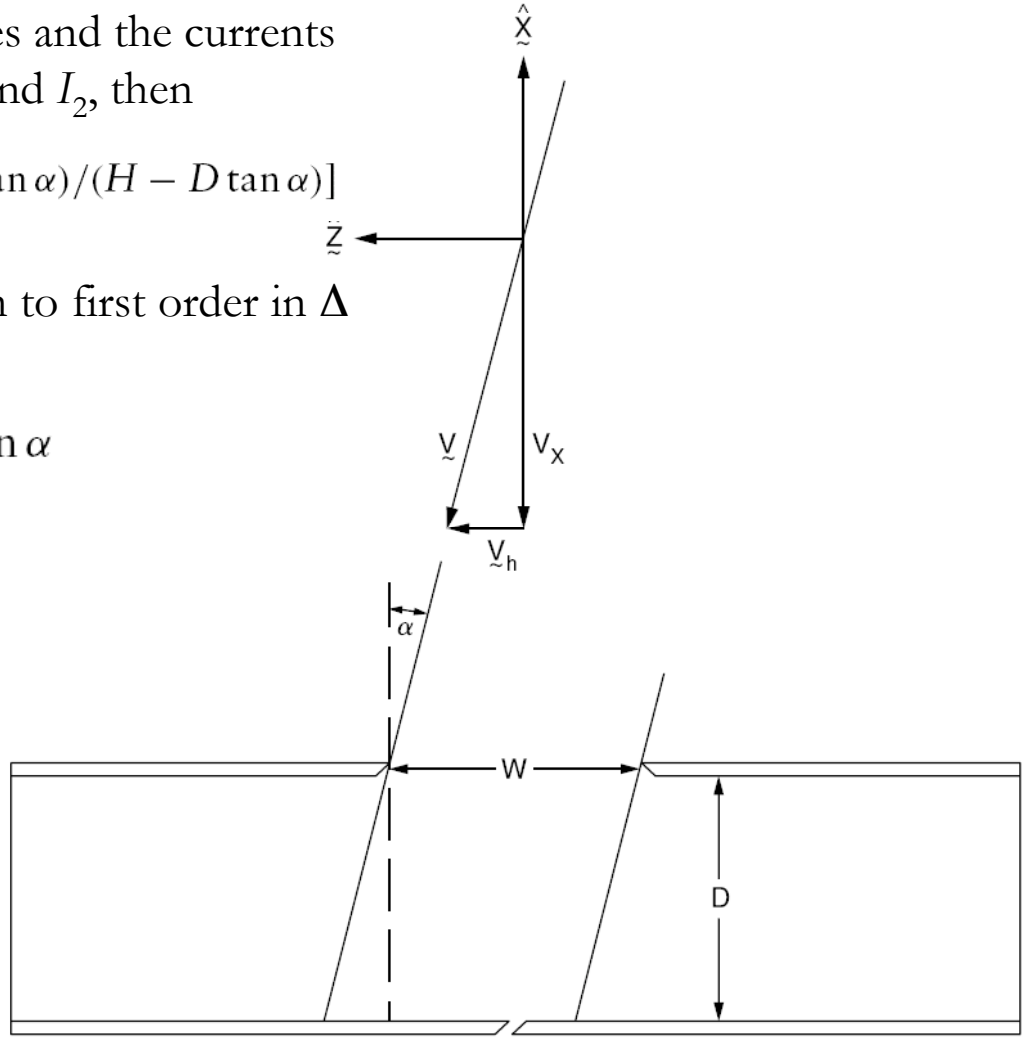

Double-Probe Electric Field Detectors

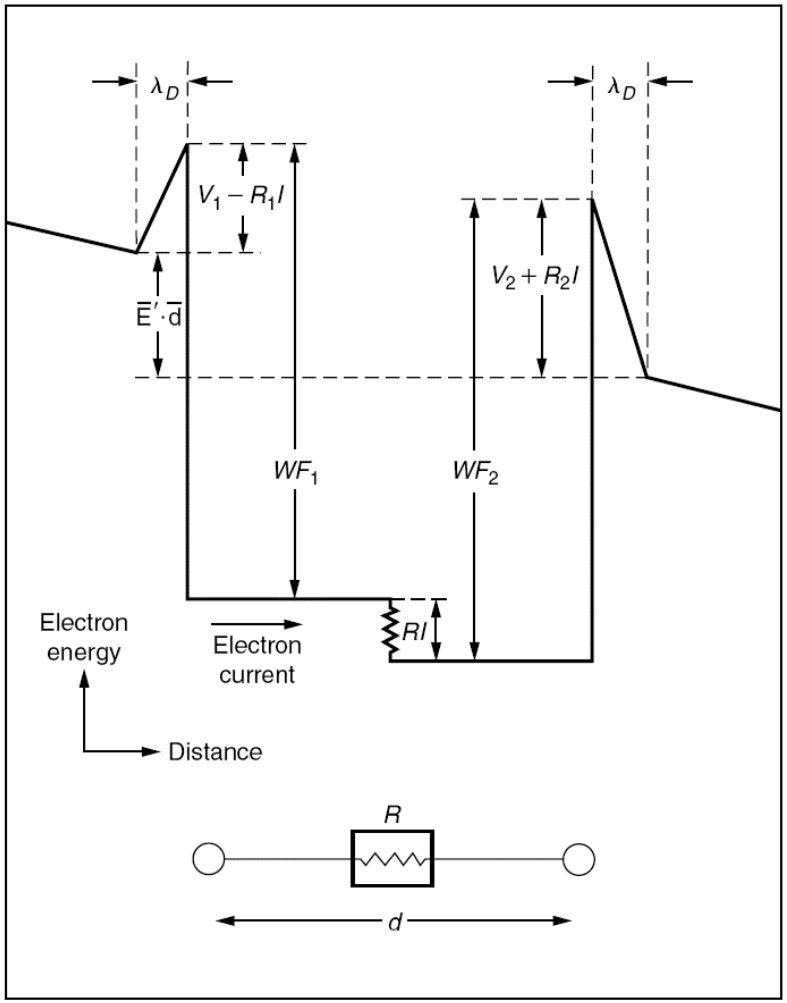

Electron potential energy as a function of position near a Langmuir double probe

The double-probe technique has been used successfully to measure electric fields on balloons, rockets, and satellites. In essence, at dc the technique makes a resistive contact to the plasma at two separated positions. If the two electrodes and their local interactions with the medium are sufficiently similar, then the difference of potential between the two electrodes equals the difference of potential between the two points in space. Dividing by the magnitude of the vector distance **d** between them yields the component of the electric field linking the two sensors.

The most symmetrical element is a sphere and many in situ electric field measurements use spherical electrodes mounted on insulating booms which are made as long as financial and mechanical constraints allow.

Double-Probe Electric Field Detectors

The length is maximized since the voltage signal V_s is proportional to $V_s = -\mathbf{E'} \cdot \mathbf{d}$, whereas the sources of error are either independent of the separation from the spacecraft or decrease drastically with separation distance. Typical boom lengths on sounding rockets range from 1 to 15m, and on satellites 100m tip-to-tip separations are commonly used.

Some of these error sources can be understood from the interaction between a single electrode and the local plasma. Consider first a floating probe, that is, one from which no current is drawn by the attached electronics. Due to their higher velocity, the flux of electrons to a given surface, nv_e , exceeds the flux of ions to the same surface, nv_i. An electrode will thus charge up negatively, repelling just enough electrons that the electron and ion fluxes are equal. For a spherical probe at rest with area A in a plasma of temperature T, with electron and ion masses m and M, the current I to the probe is given by

$$I = (Ane/4)(8k_BT/\pi M)^{1/2} - (Ane/4)(8k_BT/\pi m)^{1/2} \exp(eV_F/k_BT)$$

(Fahleson, 1967). Setting $I = 0$ for a floating probe yields $V_F = (k_BT/e) \ln(m/M)^{1/2}$

Double-Probe Electric Field Detectors

The previous schematic diagram (Mozer, 1973) shows the potentials involved when two separated electrodes, with different work functions WF_1 and WF_2, different floating potentials V_1 and V_2, and separated by a distance **d** in an external electric field **E** are connected to a differential electrometer with input resistance R. To make the measurement, a current I must be drawn by the electronics. This creates an additional potential difference at the two spheres denoted b $R_j = (\partial V/\partial I)_{V_F}$ is the dynamic resistance of the electrode-plasma contact evaluated at the floating potential. Differentiating and evaluating R at the floating potential yields $R = (k_B T/e)/I_i$

That is, the electron temperature measured in electron volts divided by the ion current to the probe yields the dynamic resistance for a floating probe. For a sphere of 100 cm2 projected collection area, moving through a plasma of temperature 0.16 eV at a velocity of 1 km/s with a density of 104 cm−3 , $R \approx 107$. Analysis of the potential diagram shows that the electrometer measures

$$RI = \left[\mathbf{E}' \cdot \mathbf{d} + (V_1 - V_2) + (WF_2 - WF_1)\right] \Big/ \left[1 + (R_1/R) + (R_2/R)\right]$$

Motion of the spacecraft across the earth's magnetic field at velocity $\mathbf{V}_s$ creates an additional vector electric field contribution since in the moving frame the field **E** is given by $\mathbf{E}' = \mathbf{E}_A + \mathbf{V}_s \times \mathbf{B}$

where $\mathbf{E}_A$ is the desired ambient electric field. Subtraction of two vectors requires accurate knowledge of $\mathbf{V}_s$ and the vehicle attitude. The magnetic field itself is usually known quite well at ionospheric heights and is not a problem in carrying out the required vector subtraction.

Barium Ion Cloud Measurements

Since the electric field is of crucial importance to the understanding of ionospheric dynamics, tracer techniques were developed in the 1960s to measure the flow velocity of the ionospheric plasma. The basic idea is to inject a small number of atoms into the medium under conditions such that the cloud is fully sunlit but observers on the ground are in darkness. For certain materials the sunlight both ionizes the material and makes it visible via a resonant scattering process. Barium vapor has proved to be the best material for this experiment and well over 100 releases have been carried out over the years at altitudes from 150 to 60,000km. To vaporize the barium metal, very high temperatures are needed, and a thermite reaction is used to attain the required heat of vaporization. As discussed in the text, small clouds are needed if the tracer aspect is important. "Small" in this case means that the height-integrated conductivity of the cloud must be less than that of the ionosphere. Following Haerendel et al. (1967), at F region altitudes the electric field is given by

$$\mathbf{E}_\perp = \frac{1+\lambda^*}{2} B \left[\hat{B} \times \mathbf{V}_\perp + \frac{1}{k_i} (\mathbf{V}_\perp - \mathbf{U}_{n\perp}) + \frac{\lambda^* - 1}{\lambda^* + 1} \mathbf{U}_{n\perp} \times \mathbf{B} \right]$$

where $\mathbf{V}_\perp$ is the velocity of the ion cloud perpendicular to $\mathbf{B}$, λ^* is the ratio of height-integrated Pedersen conductivities in the presence and in the absence of the cloud, k_i is the ratio of the gyration frequency to the collision frequencies of a barium ion, $\mathbf{U}_{n\perp}$ is the neutral wind velocity in the reference frame fixed to the earth, and $\mathbf{E}$ and $\mathbf{E}_\perp$ represent the ionospheric electric field in a frame of reference fixed to the earth in the plane perpendicular to the local magnetic field direction. For $\lambda^* = 1$ and k_i large (F region altitudes) $\mathbf{V}_\perp$ is equal to $(\mathbf{E}\times\mathbf{B})/B^2$. The method has proved to be extremely valuable for measuring electric fields in the ionosphere. This is particularly true at low latitudes, where probe techniques and drift meters must contend with satellite velocities much in excess of the plasma velocity.